Supplementary material

Enhanced charge carriers separation by bi-piezoelectric effects based on pine needle-like $BaTiO_3$/ZnO continuous nanofibers

Wanxing Zheng [a] Yufei Tang [a,b,*],Zhaowei Liu [a], Guoxin Xing [a], Kang Zhao [a,b]

a *Department of Materials Science and Engineering Xi'an University of Technology, Xi'an 710048, PR China. E-mail:* yftang@xaut.edu.cn

b *Shaanxi Province Key Laboratory of Corrosion and Protection, Xi'an University of Technology, Xi'an 710048, PR China.*

**Corresponding author.* .E-mail: yftang@xaut.edu.cn

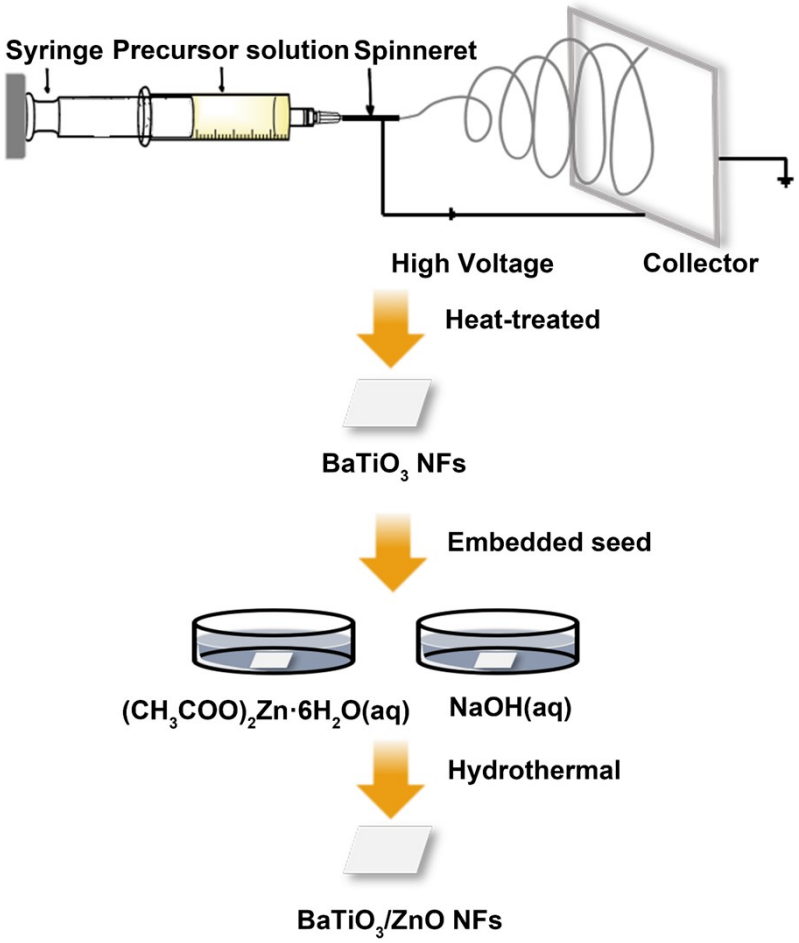

Scheme S1. The diagram of fabrication of $BaTiO_3$/ZnO continuous nanofibers.

The N_2 adsorption-desorption measurements of $BaTiO_3$/ZnO continuous nanofibers with different interface densities are shown in Fig. S1, and the corresponding specific surface area, pore volume and pore diameter are summarized in Table S1. All the isotherms are identified as type IV, with H3 hysteresis loops, suggesting their porous structure. As shown in Table S1, the BET surface area of BTZ-0.02, BTZ-0.04 and BTZ-0.06 are 14.7148, 18.8191 and 18.6058m^2/g, respectively. The last one is smaller than BTZ-0.04, which may be the numerous ZnO nanorods completely cover the $BaTiO_3$ nanofibers.

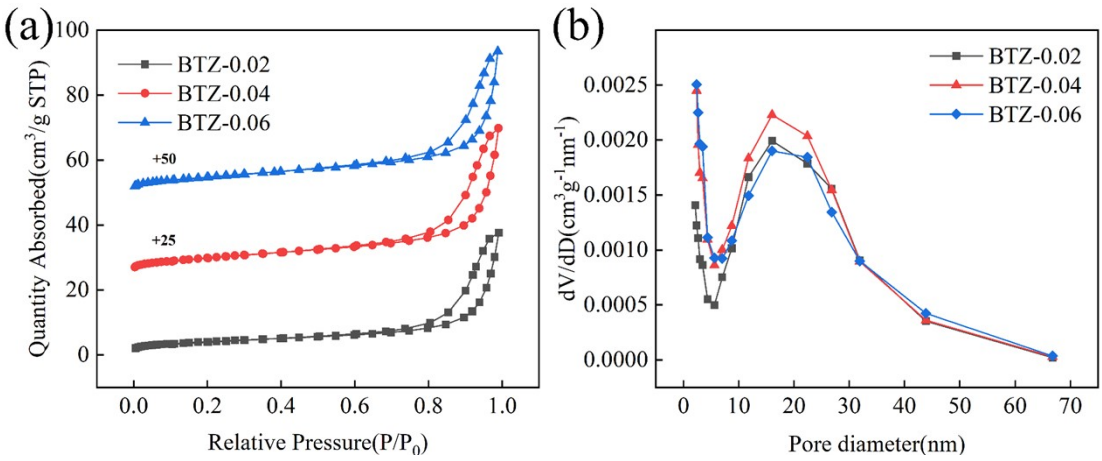

Fig. S1. (a)N_2 adsorption-desorption curve and (b) BJH pore size distribution of BTZ-series samples.

Table S1. Specific surface area, total pore volume and average pore diameter of BTZ samples

samples	S (m^2/g, BET)	Pore volume (cm^3/g, BET)	pore diameter (nm, BJH)
BTZ-0.02	14.7148	0.058226	17.4693
BTZ-0.04	18.8191	0.069292	15.6627
BTZ-0.06	18.6058	0.067268	15.2836

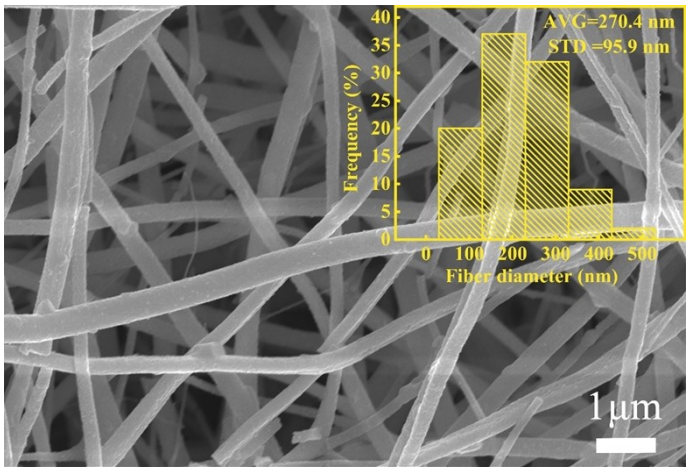

Fig. S2. SEM image of $BaTiO_3$ nanofibers and the inset is corresponding diameter distribution diagram.

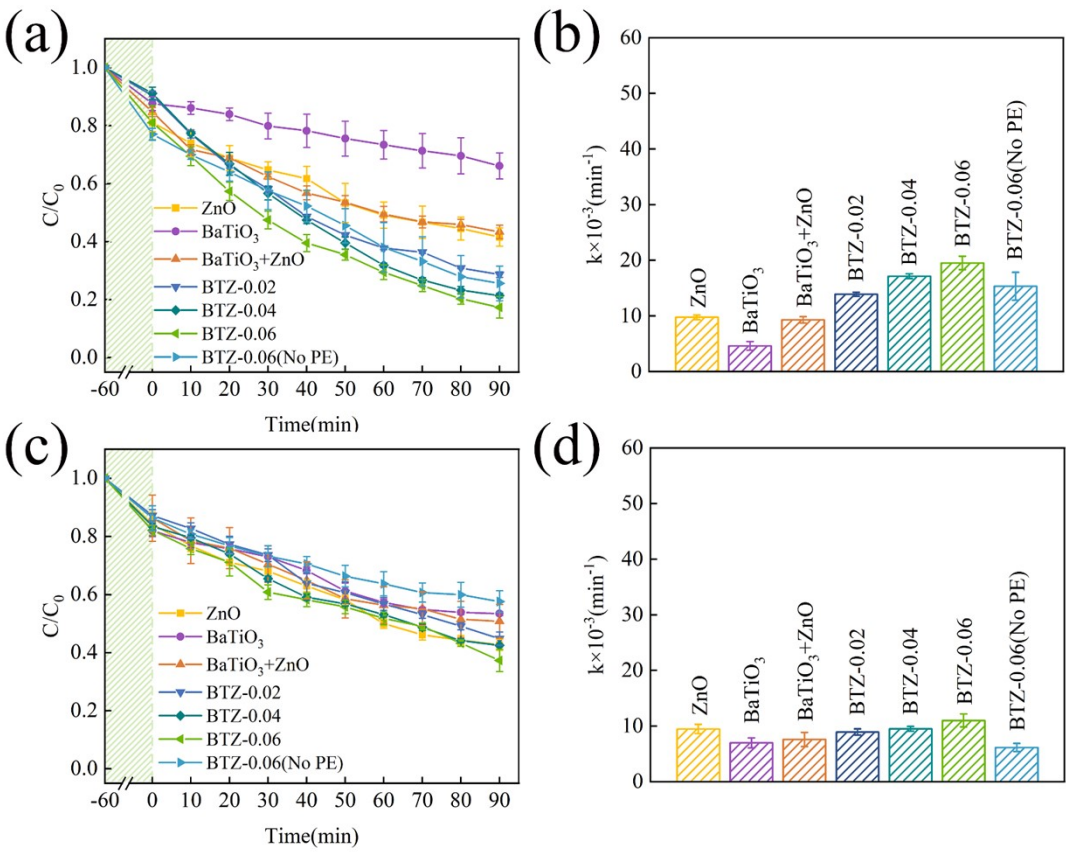

Fig. S3. The degradation curve and the corresponding comparison of degradation ratios of $BaTiO_3$/ZnO continuous nanofibers on the degradation of RhB under(a, b)light only, (c, d)ultrasonic only.

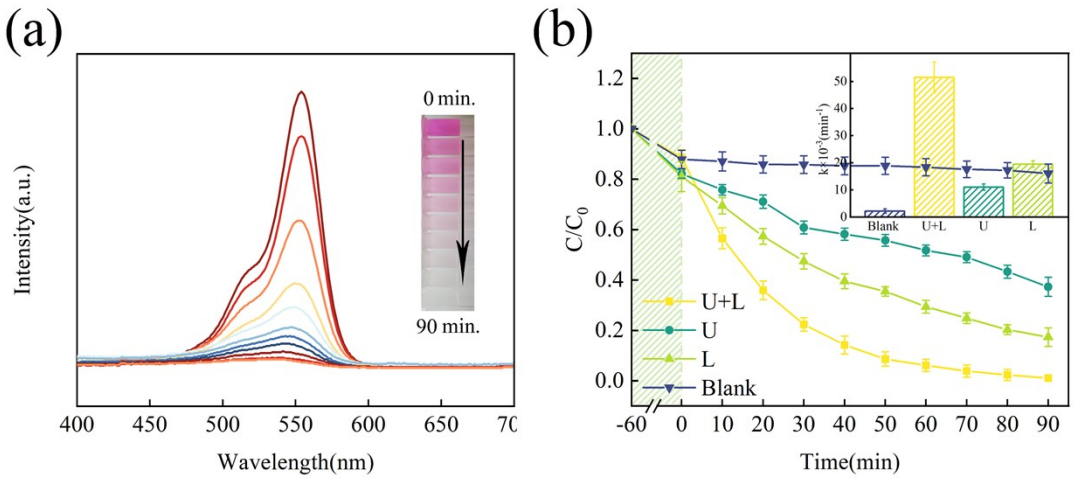

Fig. S4. (a) Catalytic behaviors for degradation of RhB by the BTZ-0.06 under UV light irradiation and ultrasonic, the ultrasound power is fixed at 120W, (b) The degradation curve of BTZ-0.06 continuous nanofibers on the degradation of RhB under different experimental conditions, the inset is corresponding comparison of reaction rate constant.

Fig.S5ii shows the SEM image of BTZ-0.08, it can be seen that ZnO almost covered $BaTiO_3$ nanofibers. In addition, the nucleation sites of ZnO on the $BaTiO_3$ nanofibers were increased due to the higher concentration of the precursors. During the hydrothermal self-assembly, the grown rods met each other and merged together, resulting in BTZ-0.08 no longer having a pine needle-like structure. In other words, ZnO in BTZ-0.08 has no one-dimensional form, which may reduce utilization of ultrasonic. Fig. S5 shows the degradation curve of BTZ-0.08 continuous nanofibers on the degradation of RhB under UV light irradiation and ultrasonic, it can be observed that the degradation reaches 97.64% after 90min. The degradation is not much different from that of BTZ-0.06(98.94%). However, the reaction rate constants(42.27×10^{-3} min^{-1}) is significantly lower than that of BTZ-0.06(51.50×10^{-3} min^{-1}), as shown in Fig. S5i. This result can be ascribed to merged ZnO makes partial of the $BaTiO_3$/ZnO composite interface ineffective.

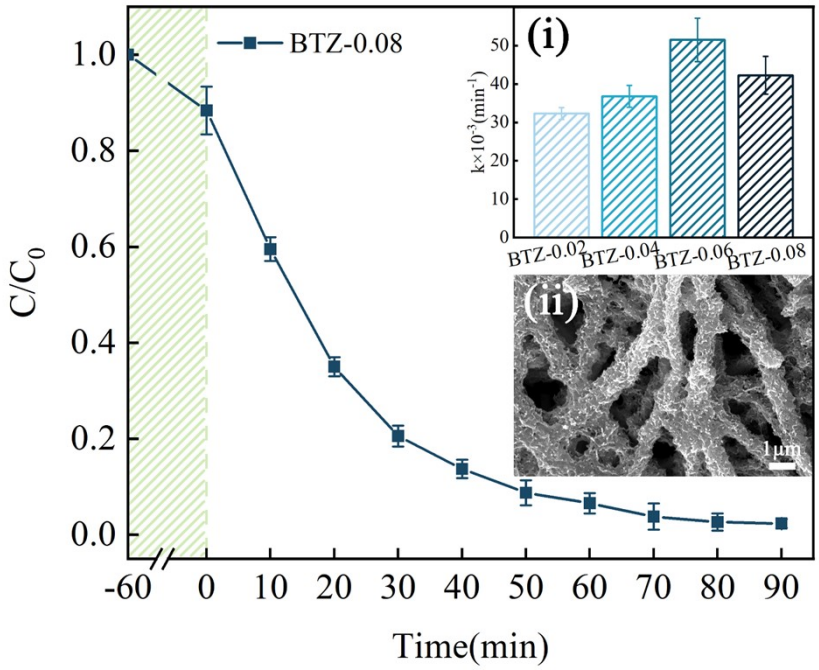

Fig. S5. The degradation curve of BTZ-0.08 continuous nanofibers on the degradation of RhB under UV light irradiation and ultrasonic. Inset (i) is the corresponding comparison of reaction rate constant, (ii) presents SEM image of BTZ-0.08 continuous nanofibers.

Fig. S6 shows the XRD patterns of the $BaTiO_3$ NFs obtained at different calcination temperatures and composite nanofibers after growing ZnO nanorods. The diffraction peaks of BTZ-0.06-700℃ are sharp and clear, and there are no double peaks at the diffraction angles around 22°, 45°, 50°, 65°, 70°, indicating that they perfectly match cubic $BaTiO_3$ (PDF#JCPDS: 31-0174). The diffraction peaks of BTZ-0.06-800℃(i.e., BTZ-0.06) has double peaks near the above diffraction angles, which indicates that $BaTiO_3$ in BTZ-0.06 is tetragonal phase.

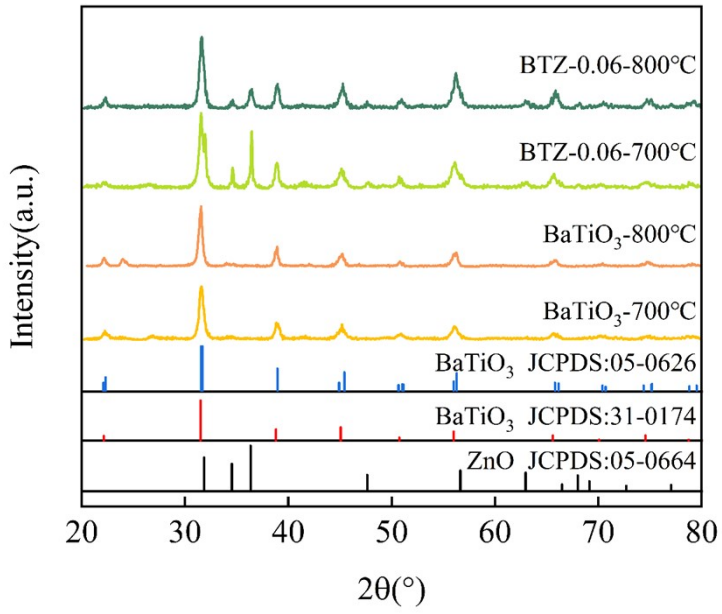

Fig. S6. XRD patterns of the $BaTiO_3$ NFs obtained at different calcination temperatures and composite nanofibers after growing ZnO nanorods.

The only difference between the fabrication of BTZ-0.06 and BTZ-0.06-700℃ is the heat treatment temperature, which has no effect on the morphology of $BaTiO_3$/ZnO. Fig. S7 shows the SEM image of the BTZ-0.06-700℃ continuous nanofibers and shown below as well. It can be observed that BTZ-0.06-700℃ still is pine needle-like

structure. Therefore, the difference between the BTZ-0.06-700℃ and BTZ-0.06 is that the $BaTiO_3$ nanofibers in the former do not possess piezoelectricity.

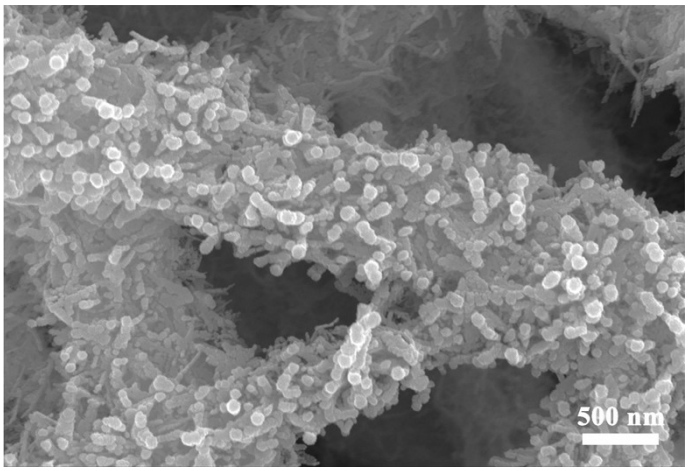

Fig. S7. SEM image of the BTZ-0.06-700℃ continuous nanofibers.

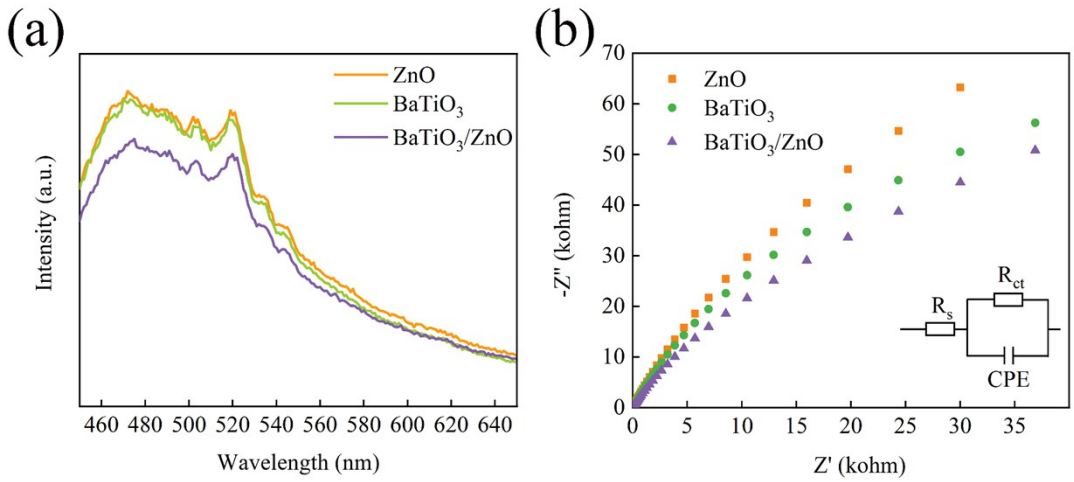

Fig. S8. (a)PL spectrum, (b)EIS curves of ZnO, $BaTiO_3$ and $BaTiO_3$/ZnO(BTZ-0.06) continuous nanofibers.

To explore the migration route of photogenerated carriers more clearly, it is necessary to clarify the energy band structure of $BaTiO_3$ and ZnO. Fig. S9a shows UV-Vis absorption diffuse reflectance spectra of ZnO, $BaTiO_3$ and $BaTiO_3$/ZnO. The intrinsic absorption edges of $BaTiO_3$ and ZnO are 386 nm and 395 nm, respectively, and $BaTiO_3$/ZnO is located between them. It's caused by heterojunction in $BaTiO_3$/ZnO. The calculated band gaps of ZnO and $BaTiO_3$ using a taucplot are shown in Fig. S9b, and are 3.18 eV and 3.32 eV, respectively. The edge positions of $BaTiO_3$ and ZnO are obtained from Fig. S8c, the valance band potential(E_{VB}) of $BaTiO_3$ and ZnO are 1.51 eV and 2.51 eV, respectively. The conduction band potential(E_{CB}) can be calculated by the empirical equation as follows:

$$E_{CB}=E_{VB}-E_g$$

The E_{CB} of $BaTiO_3$ and ZnO are calculated at about -1.81 eV and -0.69 eV, respectively. Based on this, the energy band structure of pine needle-like $BaTiO_3$/ZnO continuous nanofibers can be obtained as shown in Fig. S9d.

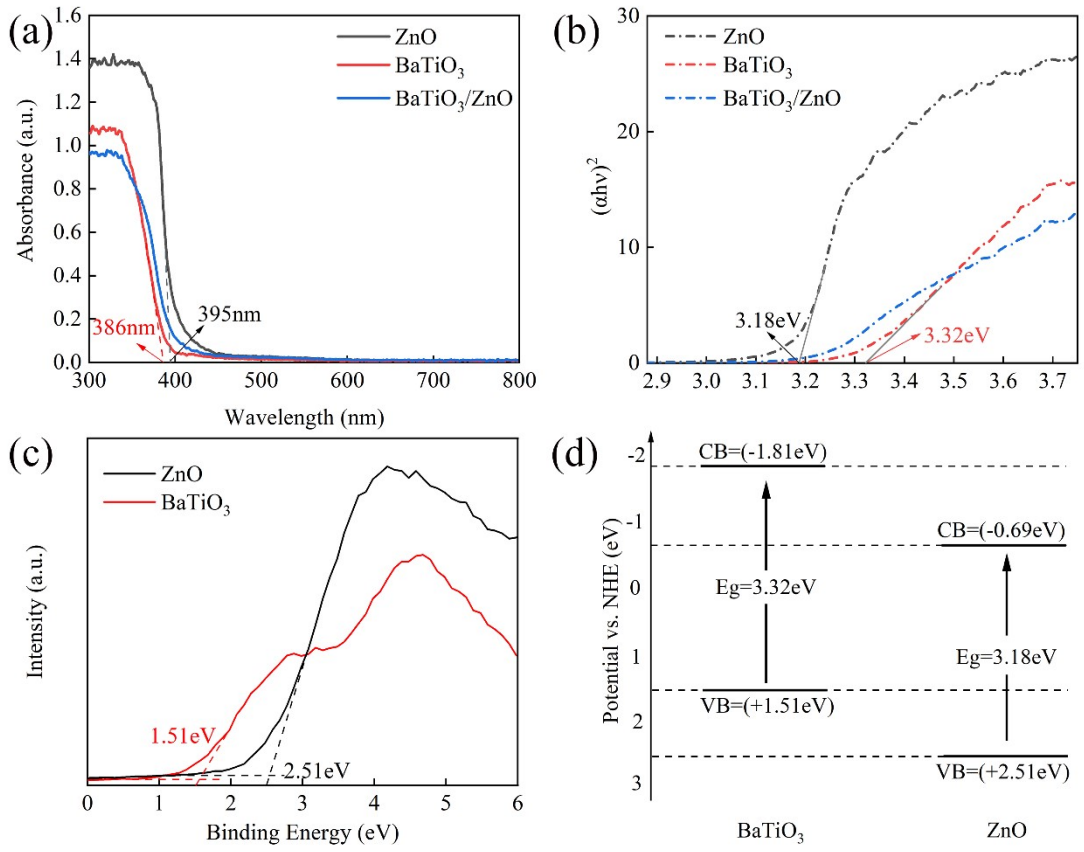

Fig. S9. Band structure of pine needle-like $BaTiO_3$/ZnO composite nanofibers: (a) Uv-vis absorption spectrum, (b) Plot of $(\alpha h\nu)^2$-hν, (c) XPS valence band spectrum of ZnO and $BaTiO_3$, (d) schematic diagram of band structure.

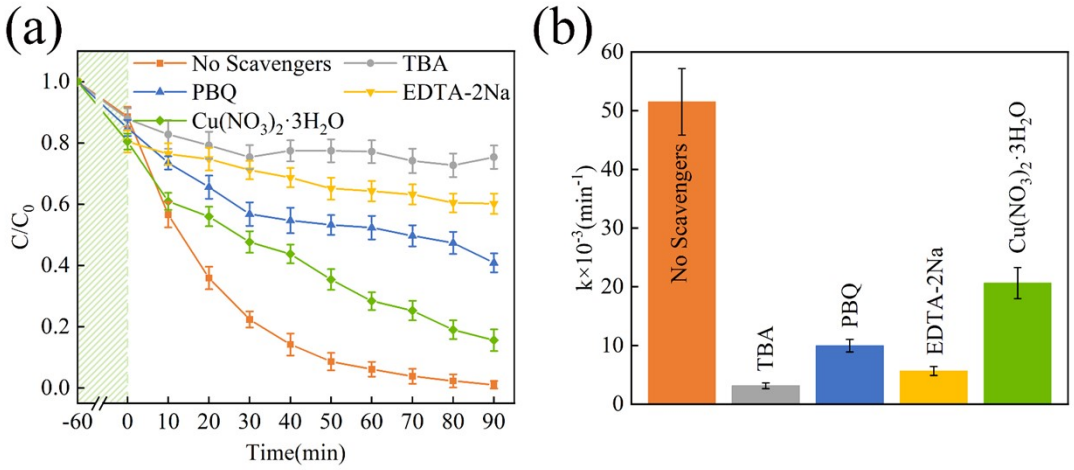

Fig. S10. (a) Piezophotocatalytic degradation with BTZ-0.06 in the presence of ·OH(TBA), $\cdot O_2^-$(PBQ), h^+(EDTA-2Na) and e^-($Cu(NO_3)_2 \cdot 3H_2O$) scavengers. (b) Comparisons of the reaction rate constants with different radicals' scavengers.

Fig. S11 shows the degradation curve of $BaTiO_3$/ZnO continuous nanofibers on the degradation of different pollutants under ultrasonic and light. Regardless of dyes or antibiotics, the pine needle-like $BaTiO_3$/ZnO continuous nanofibers can degrade 85% of pollutants, indicating no selectivity for pollutants. BTZ-series samples presents better degradation performance that BTZ-0.06. The difference between the BTZ-0.06(No PE) and BTZ-0.06 is that the $BaTiO_3$ nanofibers in the former do not possess piezoelectricity. Therefore, the bi-piezoelectric enhancement promotion mechanism works only in the BTZ-series samples. However, bi-piezoelectric-promoted photogenerated carrier separation is directly manifested with the rate of catalytic reaction, and the reaction rates for the degradation of different pollutants are summarized in Fig. 8b.

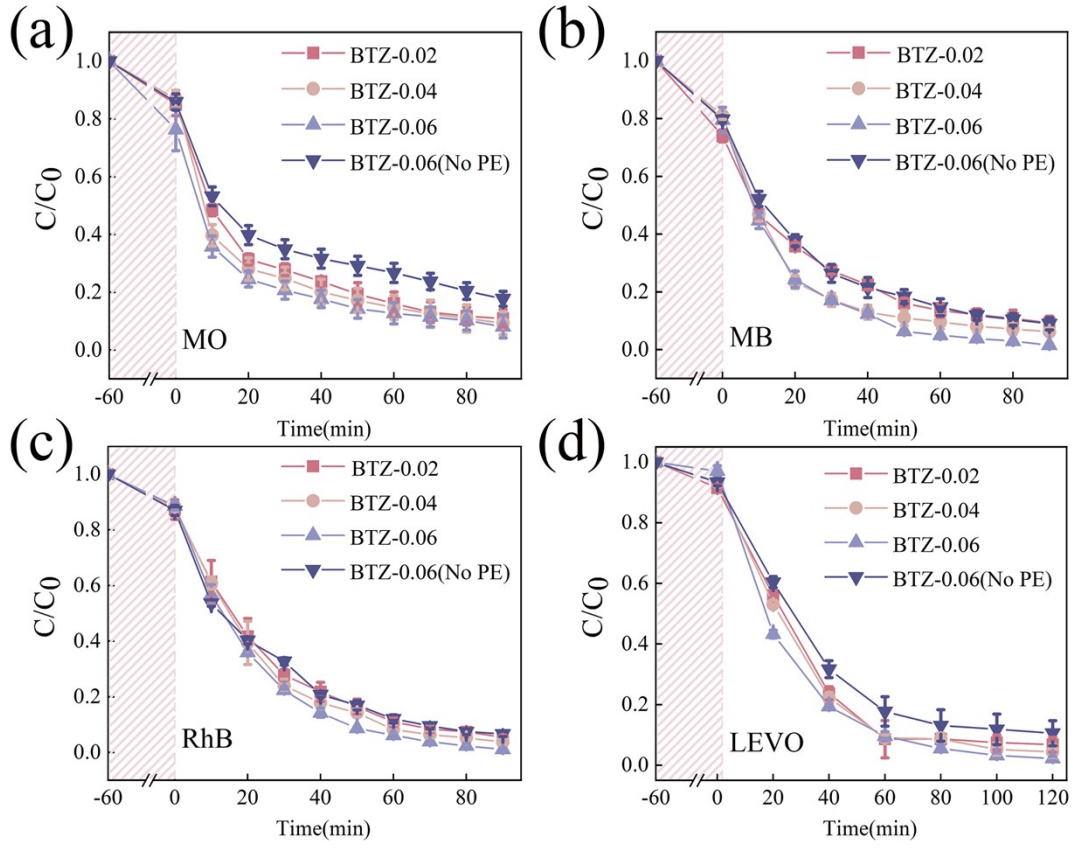

Fig. S11.The degradation curve of $BaTiO_3$/ZnO continuous nanofibers on the degradation of different pollutants under ultrasonic and light, (a)MO, (b)MB, (c)RhB, (d) LEVO.